Available online at www.sciencedirect.com

ScienceDirect

IFAC Papers Online CONFERENCE PAPER ARCHIVE

IFAC PapersOnLine 59-19 (2025) 502–507

Position and anti-drift control of large-scale curling HASEL actuators ⋆

Nelson Cisneros *, **Cristobal Ponce** *,**, **Yongxin Wu** *, **Alessandro Macchelli** ***, **Yann Le Gorrec** *, **Hector Ramirez** **

* *Université Marie et Louis Pasteur, SUPMICROTECH-ENSMM, CNRS, Institut FEMTO-ST, Besançon, France. Emails: {nelson.cisneros, cristobal.ponce, yongxin.wu, legorrec}@femto-st.fr*

** *Departamento de Electrónica, Universidad Técnica Federico Santa María, Valparaíso, Chile. Emails: {cristobal.ponces, hector.ramireze}@usm.cl*

*** *Department of Electrical, Electronic and Information Engineering, University of Bologna, Italy. Email: alessandro.macchelli@unibo.it*

Abstract: This paper addresses the position and anti-drift control of large-scale curling Hydraulically Amplified Self-Healing Electrostatic (HASEL) actuators using the Interconnection and Damping Assignment Passivity-Based Control (IDA-PBC) methodology formulated within the port-Hamiltonian systems (PHS) framework. Expanding upon previous work on low-scale models, this study adapts the control strategy to large-scale systems, ensuring its effectiveness across scales. The proposed control law retains its structure from the low-scale case, with dimensionality remaining constant despite the increased system complexity. As in the low-scale setting, the closed-loop system mitigates the drift. Numerical simulations confirm the methodology's effectiveness, demonstrating its capability to achieve precise position control and mitigate drift in large-scale systems.

Keywords: Port-Hamiltonian systems; Passivity-based Control; Nonlinear control; HASEL actuator; Soft actuator.

1. INTRODUCTION

HASEL (Hydraulically Amplified Self-Healing Electrostatic) actuators have emerged as a promising technology in soft robotics, blending the characteristics of dielectric elastomer actuators and fluid-driven systems. These actuators use electrostatic forces to generate large deformations, providing high energy efficiency, resilience to electrical failures, and versatile actuation capabilities. Their potential has been demonstrated in various applications, including bioinspired soft robotic structures and grippers, where their adaptability and performance under diverse conditions make them ideal candidates for advanced robotic systems (Kellaris et al., 2018; Tripathi et al., 2024; Kazemipour et al., 2024; Hess and Musgrave, 2024; Sanchez-Tamayo et al., 2024; Volchko et al., 2024). Curling HASEL actuators, in particular, are capable of complex bending motions, making them well-suited for adaptive and flexible robotic applications (Kellaris et al., 2021). However, one of the major challenges in deploying HASEL actuators, especially for long-term operations, is the drift effect. This phenomenon arises due to material fatigue, electrostatic force variations, and mechanical hysteresis, causing the actuator's position or state to gradually shift over time (Sîrbu et al., 2023; Prodromakis and Papavassiliou, 2009). Drift can significantly compromise the precision and stability of the actuator, particularly in high-precision applications where reliable and accurate control is essential.

The modelling and control of curling HASEL actuators have gained considerable attention, with the port-Hamiltonian systems (PHS) framework emerging as a robust tool for capturing the dynamics of such systems. PHS offers a modular, energy-based approach to modelling interconnected systems while preserving their physical properties (Duindam et al., 2009). In previous studies, we developed low-scale models of curling HASEL actuators (Cisneros et al., 2024), which effectively captured the coupling between mechanical, electrical and fluid domains. These models were augmented with an Interconnection and Damping Assignment Passivity-Based Control (IDA-PBC) methodology that aimed to modify the actuator's equilibrium positions and mitigate drift effects.

Expanding upon this foundational work, we recently proposed a large-scale model of curling HASEL actuators (Ponce et al., 2024), incorporating a discretised beam structure to accurately represent the mechanical behaviour while retaining the PHS framework. This large-scale model offers new challenges and opportunities for the application of advanced control techniques. In this context, we aim to determine whether the control strategies developed

⋆ The authors acknowledge financial support from: Chilean ANID projects Becas/ Doctorado Nacional/ 2021-21211290, ECOS 220040, FONDECYT 1231896, BASAL AFB240002; the French ISITE-BFC project - CPHS2D - ANR-15-IDEX-0003, EIPHI Graduate School ANR-17-EURE-0002, IMPACTS Project ANR-21-CE48-0018; and the European MSCA Project MODCONFLEX 101073558.

10.1016/j.ifacol.2025.11.084

for low-scale models remain effective when extended to large-scale systems. The contribution of this paper is the extension of the IDA-PBC methodology to the control of large-scale curling HASEL actuators, demonstrating that the control law effective for low-scale models is directly applicable to larger systems. Despite the increase in system scale, the structure of the controller remains unchanged, with the dimensionality of the control law unaffected by the larger state space. This approach effectively addresses position control and drift mitigation.

The paper is organised as follows: Section 2 reviews the large-scale model presented in (Ponce et al., 2024). Section 3 introduces the proposed control law based on IDA-PBC. Section 4 presents simulation results, illustrating the controller's performance and providing a comparative analysis. Finally, Section 5 summarises the findings and discusses future research directions.

2. CURLING HASEL ACTUATOR

The curling HASEL actuator is made up of a polymer pouch containing a dielectric liquid, with one-half of the pouch covered by a pair of electrodes attached to a strain-limiting layer. When an electric field is applied to the electrodes, Maxwell stress is generated, exerting force on the shell and causing the dielectric liquid to move within it. This movement creates hydraulic pressure that deforms the pouch, and the strain-limiting layer directs this deformation into a bending motion in the actuator (Rothemund et al., 2021). The drift effect, linked to the charge retention phenomenon as described in the literature (Rumley et al., 2022; Xiong et al., 2024), appears as a positional drift when a constant voltage is applied to the actuator. The retained charge within the actuator's materials produces an internal electric field that opposes the applied external field that creates Maxwell stress, resulting in the observed drift effect (see Figure 1).

2.1 Model of the strain limiting layer

According with the large-scale model proposed in (Ponce et al., 2024), the strain limiting layer is modelled with a discretized beam model.

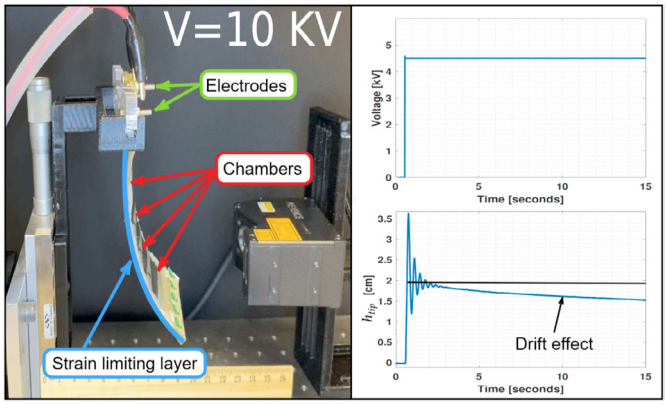

Fig. 1. Curling HASEL actuator and drift effect on tip position h_{tip}.

In this paper, the beam model corresponds to a discretized Euler-Bernoulli cantilever beam given by:

$$M_b\ddot{q} + D_b\dot{q} + K_b q = 0, \tag{1}$$

where the vector $q = [\hat{v}_0^\top \quad \hat{\psi}^\top]^\top \in \mathbb{R}^{2N}$ encompasses all degrees of freedom related to the vertical and angular deformation (according with the mesh in Figure 2), and the matrices M_b, D_b, $K_b \in \mathbb{R}^{2N\times 2N}$ are the mass, damping and stiffness matrices, respectively. Assuming Rayleigh damping condition, $D_b = a_M M_b + a_K K_b$ with $a_M, a_K \in \mathbb{R}$ two real constants determined experimentally.

To couple the beam model with the low-scale HASEL model in (Cisneros et al., 2024) we permute q such that is organized as follows:

$$\hat{q} = \hat{T}q, \quad \rightarrow \quad \hat{q} = \begin{bmatrix} \hat{v}_0 \\ \hat{\psi}_f \\ \hat{\psi}_c \end{bmatrix}, \tag{2}$$

where $\hat{T} \in \mathbb{R}^{2N\times 2N}$ is a permutation matrix, $\hat{\psi}_c \in \mathbb{R}^{\ell}$ is the vector that collects all the angles associated with the nodes at the center positions of the ℓ chambers, and $\hat{\psi}_f \in \mathbb{R}^{N-\ell}$ gathers all other *free* angles (not connected to volume conservation) (see Figure 3.a). With the above, the mass, damping and stiffness matrices are redefined as:

$$\hat{M}_b = \hat{T}M_b\hat{T}^\top, \quad \hat{D}_b = \hat{T}D_b\hat{T}^\top, \quad \hat{K}_b = \hat{T}K_b\hat{T}^\top,$$

respectively, where each one can be partitioned as:

$$\hat{M}_b = \begin{bmatrix} \hat{M}_{11} & \hat{M}_{12} & \hat{M}_{13} \\ \hat{M}_{12} & \hat{M}_{22} & \hat{M}_{23} \\ \hat{M}_{13} & \hat{M}_{12} & \hat{M}_{33} \end{bmatrix}, \quad \hat{D}_b = \begin{bmatrix} \hat{D}_{11} & \hat{D}_{12} & \hat{D}_{13} \\ \hat{D}_{12} & \hat{D}_{22} & \hat{D}_{23} \\ \hat{D}_{13} & \hat{D}_{12} & \hat{D}_{33} \end{bmatrix}, \tag{3}$$

and similarly for $\hat{K}_b$. Lastly, from Figure 2, it can be observed that the tip position h_{tip} of the curling HASEL model is represented by the degree of freedom $h_{tip} = \hat{v}_0^N$.

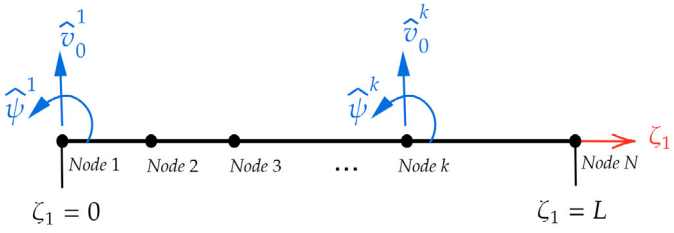

Fig. 2. Mesh, nodes and degrees of freedom.

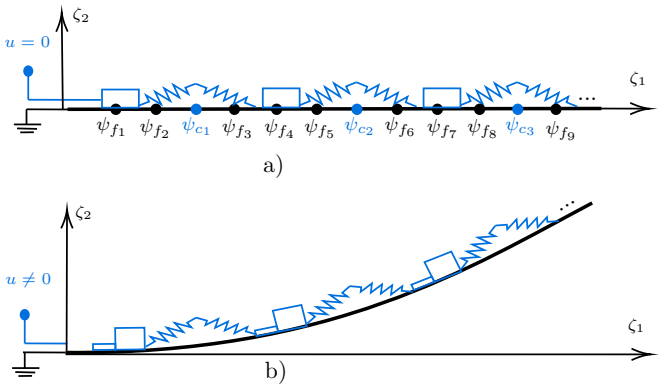

Fig. 3. (a) Large-scale actuator (voltage $u = 0$) (b) Large-scale actuator (voltage $u \neq 0$).

2.2 Chamber representation

As illustrated in Figure 4, each actuator's chamber is separated in two main parts. The active part in the left has two parallel electrodes that collapse when high voltage u is applied. The passive compartment's shape is assumed as an isosceles triangle. When high voltage is applied the liquid in the active compartment is transferred to the passive compartment causing the angular deformation of the actuator.

In Figure 4 we can identify geometrical and physical variables. From the geometry, X_h represents the constant distance between the unzipped electrodes, L_e is the constant length of the electrodes, l_e^i is the variable length of the zipped electrodes, L_v is the constant length of the bottom side of the passive compartment, $\frac{1}{2}(l_p^i - L_p)$ is the elongation of the linear springs K_l^i with L_p its natural length, δ_i is an internal angle, and A_s^i is the area of the passive compartment. From the physical point of view, the resistance of the fluid inside the chamber is characterized by the torsional spring K_f^i, K_l^i model the resistance of the upper layer, C_i is the equivalent capacitance, r_i and R_i are the equivalent resistances, and L_i the equivalent inductance.

The expressions of the geometric constraints in each chamber due to the conservation of volume are given by:

$$A_T = A_s^i + X_h(L_e - l_e^i), \tag{4}$$

$$A_s^i(\hat{\psi}_{c_i}, l_p^i) = \frac{1}{4} L_v l_p^i \sin(\delta_i(\hat{\psi}_{c_i}, l_p^i)), \tag{5}$$

$$\delta_i(\hat{\psi}_{c_i}, l_p^i) = \frac{\pi + \hat{\psi}_{c_i}}{2} - \sin^{-1}\left(\frac{L_v}{l_p^i}\sin\left(\frac{\pi - \hat{\psi}_{c_i}}{2}\right)\right), \tag{6}$$

$$l_e^i(\hat{\psi}_{c_i}, l_p^i) = \left(L_e - \frac{A_T}{X_h}\right) + \frac{L_v}{4X_h} l_p^i \sin\left(\delta_i(\hat{\psi}_{c_i}, l_p^i)\right), \tag{7}$$

where A_T is the total constant area in the plane. The expression for the nonlinear capacitor is given by:

$$C_i(\hat{\psi}_{c_i}, l_p^i) = \frac{\epsilon_0 \epsilon_r w l_e^i(\hat{\psi}_{c_i}, l_p^i)}{2h_f} + \frac{\epsilon_0 \epsilon_r w (L_e - l_e^i(\hat{\psi}_{c_i}, l_p^i))}{2h_f + X_h}, \tag{8}$$

with h_f the thickness of the film, w is the width of the actuator, ϵ_0 and ϵ_r the vacuum and relative permittivity, respectively.

2.3 Large-scale PHS model of the curling HASEL actuator

Defining the vectors: $l_p = [l_p^1, \ldots, l_p^\ell] \in \mathbb{R}^\ell$ as the vector that gathers the elongation of the linear springs, $\phi = [\phi^1, \ldots, \phi^\ell] \in \mathbb{R}^\ell$ as the vector that gathers the magnetic flux in the inductors L_i, $Q = [Q^1, \ldots, Q^\ell] \in \mathbb{R}^\ell$ as the vector that gathers the charge in the capacitors C_i, and:

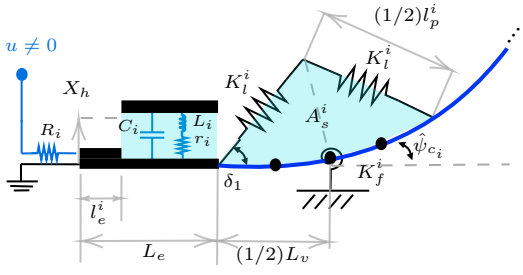

Fig. 4. Chamber scheme.

$$\hat{p} = \hat{M}_b \dot{\hat{q}} = [\hat{p}_{v_0}^\top \;\; \hat{p}_{\psi_f}^\top \;\; \hat{p}_{\psi_c}^\top]^\top \in \mathbb{R}^{2N}$$

as the linear momentum vector, together with:

$$d = \text{diag}\{\tfrac{2A_s^1}{l_p^1}, \ldots, \tfrac{2A_s^\ell}{l_p^\ell}\} \in \mathbb{R}^{\ell \times \ell}$$

as the coupling matrix, the large-scale PHS model of the culing HASEL actuator presented in (Ponce et al., 2024) is given by:

$$\begin{aligned} \dot{x} &= [J(x) - R(x)]\nabla_x H(x) + G(x)u \\ y &= G(x)^\top \nabla_x H(x) \end{aligned} \tag{9}$$

$$H(x) = H_b(\hat{p}, \hat{q}) + H_e(l_p, \phi, Q, \hat{\psi}_c) + H_f(\hat{\psi}_c), \tag{10}$$

with:

$$x = \left[\hat{p}_{v_0}^\top \; \hat{p}_{\psi_f}^\top \; \hat{p}_{\psi_c}^\top \mid \hat{v}_0^\top \; \hat{\psi}_f^\top \; \hat{\psi}_c^\top \mid l_p^\top \; \phi^\top \; Q^\top\right]^\top \in \mathbb{R}^{4N+3\ell},$$

and

$$J - R = \left[\begin{array}{ccc|ccc|ccc} -\hat{D}_{11} & -\hat{D}_{12} & -\hat{D}_{13} & -I_N & 0 & 0 & 0 & 0 & 0 \\ -\hat{D}_{12}^\top & -\hat{D}_{22} & -\hat{D}_{23} & 0 & -I_{N-\ell} & 0 & 0 & 0 & 0 \\ -\hat{D}_{13}^\top & -\hat{D}_{23}^\top & -\hat{D}_{33} & 0 & 0 & -I_\ell & -\eta\, d & 0 & 0 \\ \hline I_N & 0 & 0 & 0 & 0 & 0 & 0 & 0 & 0 \\ 0 & I_{N-\ell} & 0 & 0 & 0 & 0 & 0 & 0 & 0 \\ 0 & 0 & I_\ell & 0 & 0 & 0 & 0 & 0 & 0 \\ \hline 0 & 0 & d^\top \eta^\top & 0 & 0 & 0 & 0 & 0 & 0 \\ 0 & 0 & 0 & 0 & 0 & 0 & 0 & -r & I_\ell \\ 0 & 0 & 0 & 0 & 0 & 0 & 0 & -I_\ell & -R_e^{-1} \end{array}\right] \tag{11}$$

$$G(x) = \left[0\;0\;0 \mid 0\;0\;0 \mid 0\;0\;(R_e^{-1}\gamma(\hat{\psi}_c))^\top\right]^\top, \tag{12}$$

where $\eta = \text{diag}\{\eta_1, \ldots, \eta_\ell\} \in \mathbb{R}^{\ell \times \ell}$ is a correction factor matrix, $r = \text{diag}\{r_1, \ldots, r_\ell\} \in \mathbb{R}^{\ell \times \ell}$ and $R_e = \text{diag}\{R_1, \ldots, R_\ell\} \in \mathbb{R}^{\ell \times \ell}$ are resistance matrices, I_N, $I_{N-\ell}$ and I_ℓ are identity matrices, and $\gamma(\hat{\psi}_c) \in \mathbb{R}^\ell$ is given by:

$$\gamma(\hat{\psi}_c) = \begin{bmatrix} \alpha\cos(\beta\hat{\psi}_{c_1}) \\ \vdots \\ \alpha\cos(\beta\hat{\psi}_{c_\ell}) \end{bmatrix}, \tag{13}$$

where $\alpha, \beta \in \mathbb{R}$ are constant parameters identified experimentally. The total energy of the system is given by the Hamiltonian function $H(x) > 0 \in \mathbb{R}$ in (10), where:

$$H_b = \frac{1}{2}\hat{p}^\top \hat{M}_b^{-1}\hat{p} + \frac{1}{2}\hat{q}^\top \hat{K}_b \hat{q}, \tag{14}$$

$$H_e = \frac{1}{4}(l_p - L_p)^\top K_l (l_p - L_p) + \frac{1}{2}\phi^\top L_{ind}^{-1}\phi + \frac{1}{2}Q^\top C^{-1} Q, \tag{15}$$

$$H_f = \frac{1}{2}\hat{\psi}_c^\top K_f \hat{\psi}_c, \tag{16}$$

where $K_l = \text{diag}\{K_l^1, \ldots, K_l^\ell\} \in \mathbb{R}^{\ell \times \ell}$ is the stiffness matrix of the upper layer, $L_{ind} = \text{diag}\{L_1, \ldots, L_\ell\} \in \mathbb{R}^{\ell \times \ell}$ is the inductance matrix, and $C = \text{diag}\{C_1, \ldots, C_\ell\} \in \mathbb{R}^{\ell \times \ell}$ is the capacitance matrix.

3. CONTROLLER DESIGN

This section describes the controller design based on the Interconnection and Damping Assignment-Passivity Based Control (IDA-PBC) methodology. The objective is to achieve a desired beam position while mitigating the drift effect, a characteristic limitation of this type of actuator.

3.1 Controller design via IDA-PBC

The IDA-PBC methodology is a powerful tool for designing asymptotically stabilizing controllers for PHS (Ortega et al., 2002). This method aims to transform the open-loop system (9) into the desired closed-loop system (17) by means of the control input $u = \beta(x)$. The desired closed-loop system is expressed as:

$$\dot{x} = [J_d(x) - R_d(x)]\nabla_x H_d(x), \tag{17}$$

where J_d is the desired interconnection matrix, satisfying $J_d = -J_d^\top$, R_d is the desired damping matrix with $R_d = R_d^\top \geq 0$, and $H_d(x) > 0$ is the desired energy function. The desired energy function $H_d(x)$ satisfies the matching condition:

$$G^\perp(J_d - R_d)\nabla_x H_d = G^\perp(J - R)\nabla_x H, \tag{18}$$

where $G^\perp$ is a full-rank left annihilator of G, i.e. , $G^\perp G = 0$. Additionally, the Hamiltonian function $H_d(x)$ is designed such that:

$$x^* = arg\min H_d(x), \tag{19}$$

with x^* the desired equilibrium to be stabilized. If the matching condition (18) is satisfied, the control law $u = \beta(x)$ is given by:

$$\beta(x) = G^\dagger\left[(J_d - R_d)\nabla_x H_d - (J - R)\nabla_x H\right], \tag{20}$$

where $G^\dagger = (G^\top G)^{-1}G^\top$ is the pseudoinverse of G.

3.2 Position and anti-drift control of HASEL actuator

To impose a desired equilibrium configuration x^*, it is essential to identify the equilibrium points that the system (9) can achieve. This is done by numerically solving:

$$\dot{x} = [J(x^*) - R(x^*)]\nabla_x H(x^*) + G(x^*)u^* = 0, \tag{21}$$

where u^* varies between 0 [kV] and 10 [kV], subject to the actuator's physical constraints. For each scenario, x^* is computed, and the equilibrium states are plotted against the tip position $h_{tip} = \hat{v}_0^N$, facilitating the correlation between the states and the desired tip position. Figures 5 and 6 respectively illustrate the equilibrium angles $\hat{\psi}_c^*$ and the charge Q^* associated with each chamber, consistent with the desired equilibrium tip position h_{tip}^*.

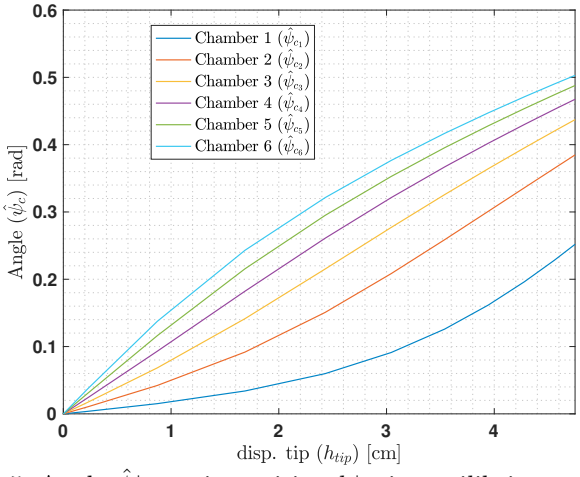

Fig. 5. Angle $\hat{\psi}_{c_i}^*$ vs tip position h_{tip}^* in equilibrium.

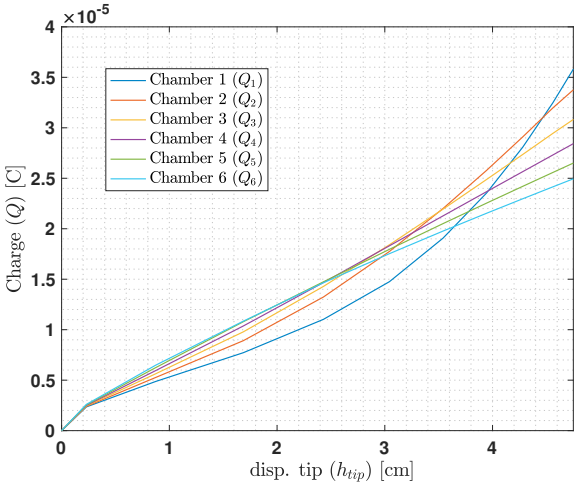

Fig. 6. Charge Q_i^* vs tip position h_{tip}^* in equilibrium.

Similarly to the controller proposed for the low-scale model in (Cisneros et al., 2024), the desired closed-loop system for the large-scale actuator is proposed as:

$$J_d - R_d = \left[\begin{array}{ccc|ccc|ccc} -r_{11} & -r_{12} & -r_{13} & -J_1 & 0 & 0 & 0 & 0 & 0 \\ -r_{12}^\top & -r_{22} & -r_{23} & 0 & -J_2 & 0 & 0 & 0 & 0 \\ -r_{13}^\top & -r_{23}^\top & -r_{33} & 0 & 0 & -J_3 & -J_4 & -J_5 & \alpha_1 \\ \hline J_1^\top & 0 & 0 & 0 & 0 & 0 & 0 & 0 & 0 \\ 0 & J_2^\top & 0 & 0 & 0 & 0 & 0 & 0 & 0 \\ 0 & 0 & J_3^\top & 0 & 0 & 0 & 0 & 0 & \alpha_2 \\ \hline 0 & 0 & J_4^\top & 0 & 0 & 0 & 0 & 0 & \alpha_3 \\ 0 & 0 & J_5^\top & 0 & 0 & 0 & 0 & 0 & \alpha_4 \\ 0 & 0 & -\alpha_1^\top & 0 & 0 & -\alpha_2^\top & -\alpha_3^\top & -\alpha_4^\top & -r_{55} \end{array}\right] \tag{22}$$

$$\begin{aligned} H_d = & \frac{c_1}{2}(\hat{q} - \hat{q}^*)^\top(\hat{q} - \hat{q}^*) + \frac{c_2}{2}(l_p - l_p^*)^\top(l_p - l_p^*) + \cdots \\ & \frac{c_3}{2}(\phi - \phi^*)^\top(\phi - \phi^*) + \frac{c_4}{2}(Q - Q^*)^\top(Q - Q^*) \\ & \cdots + \frac{1}{2}\hat{p}^\top \hat{M}_b^{-1}\hat{p}, \end{aligned} \tag{23}$$

where J_1, J_2, J_3, J_4, J_5, α_1, α_2, α_3, α_4, r_{11}, r_{22}, r_{33}, r_{12}, r_{13}, r_{23} and r_{55} are structural design parameters (matrices), and c_1, c_2, c_3 and c_4 are energy design parameters (scalars). With the above, $\nabla_x H_d(x)$ is given by:

$$\nabla_x H_d = \left[\begin{array}{c} \nabla_{\hat{p}_{v_0}} H_d \\ \nabla_{\hat{p}_{\psi_f}} H_d \\ \nabla_{\hat{p}_{\psi_c}} H_d \\ \hline \nabla_{\hat{v}_0} H_d \\ \nabla_{\hat{\psi}_f} H_d \\ \nabla_{\hat{\psi}_c} H_d \\ \hline \nabla_{l_p} H_d \\ \nabla_{\phi} H_d \\ \nabla_{Q} H_d \end{array}\right] = \left[\begin{array}{c} \begin{bmatrix} \hat{M}_{11} & \hat{M}_{12} & \hat{M}_{13} \\ \hat{M}_{12} & \hat{M}_{22} & \hat{M}_{23} \\ \hat{M}_{13} & \hat{M}_{12} & \hat{M}_{33} \end{bmatrix}^{-1} \begin{bmatrix} \hat{p}_{v_0} \\ \hat{p}_{\psi_f} \\ \hat{p}_{\psi_c} \end{bmatrix} \\ \hline c_1(\hat{v}_0 - \hat{v}_0^*) \\ c_1(\hat{\psi}_f - \hat{\psi}_f^*) \\ c_1(\hat{\psi}_c - \hat{\psi}_c^*) \\ \hline c_2(l_p - l_p^*) \\ c_3(\phi - \phi^*) \\ c_4(Q - Q^*) \end{array}\right]. \tag{24}$$

From the matching condition (18), together with the left annihilator $G^\perp$ given by:

$$G^{\perp} = \begin{bmatrix} I_N & 0 & 0 & 0 & 0 & 0 & 0 & 0 & 0 \\ 0 & I_{N-\ell} & 0 & 0 & 0 & 0 & 0 & 0 & 0 \\ 0 & 0 & I_\ell & 0 & 0 & 0 & 0 & 0 & 0 \\ 0 & 0 & 0 & I_N & 0 & 0 & 0 & 0 & 0 \\ 0 & 0 & 0 & 0 & I_{N-\ell} & 0 & 0 & 0 & 0 \\ 0 & 0 & 0 & 0 & 0 & I_\ell & 0 & 0 & 0 \\ 0 & 0 & 0 & 0 & 0 & 0 & I_\ell & 0 & 0 \\ 0 & 0 & 0 & 0 & 0 & 0 & 0 & I_\ell & 0 \end{bmatrix}, \tag{25}$$

the structural design parameters J_1, J_2, J_3, J_4, J_5 can be obtained and are given by:

$$\begin{aligned} J_1 &= I_N, \\ J_2 &= I_{N-\ell}, \\ J_3 &= \text{diag}(\text{diag}(\nabla_{\hat{p}_{\psi_c}} H_d)^{-1}[\nabla_{\hat{p}_{\psi_c}} H_d - \alpha_2 c_4 (Q - Q^*)]), \\ J_4 &= \text{diag}(\text{diag}(\nabla_{\hat{p}_{\psi_c}} H_d)^{-1}[\eta\, d\, \nabla_{\hat{p}_{\psi_c}} H_d - \alpha_3 c_4 (Q - Q^*)]), \\ J_5 &= \text{diag}(\text{diag}(\nabla_{\hat{p}_{\psi_c}} H_d)^{-1}[\nabla_{\hat{p}_{\psi_c}} H_d - \alpha_4 c_4 (Q - Q^*)]). \end{aligned}$$

In addition, assigning r_{12}, r_{13} and r_{23}, the terms r_{11}, r_{22} and r_{33} are then expressed as:

$$\begin{aligned} r_{11} = \text{diag}(\text{diag}(\nabla_{\hat{p}_{v_0}} H_d)^{-1}[&-r_{12}\nabla_{\hat{p}_{\psi_f}} H_d - r_{13}\nabla_{\hat{p}_{\psi_c}} H_d \\ &+ \hat{D}_{11}\nabla_{\hat{p}_{v_0}} H_d + \hat{D}_{12}\nabla_{\hat{p}_{\psi_f}} H_d + \hat{D}_{13}\nabla_{\hat{p}_{\psi_c}} H_d \\ &+ \nabla_{\hat{v}_0} H - c_1 J_1 (\hat{v}_0 - {\hat{v}_0}^*)]), \\ r_{22} = \text{diag}(\text{diag}(\nabla_{\hat{p}_{\psi_f}} H_d)^{-1}[&-r_{12}^\top \nabla_{\hat{p}_{v_0}} H_d - r_{23}\nabla_{\hat{p}_{\psi_c}} H_d \\ &+ \hat{D}_{12}^\top \nabla_{\hat{p}_{v_0}} H_d + \hat{D}_{22}\nabla_{\hat{p}_{\psi_f}} H_d + \hat{D}_{23}\nabla_{\hat{p}_{\psi_c}} H_d \\ &+ \nabla_{\hat{\psi}_f} H - c_1 J_2 (\hat{\psi}_f - \hat{\psi}_f^*)]), \\ r_{33} = \text{diag}(\text{diag}(\nabla_{\hat{p}_{\psi_c}} H_d)^{-1}[&-r_{13}^\top \nabla_{\hat{p}_{v_0}} H_d - r_{23}^\top \nabla_{\hat{p}_{\psi_f}} H_d \\ &+ \hat{D}_{13}^\top \nabla_{\hat{p}_{v_0}} H_d + \hat{D}_{23}^\top \nabla_{\hat{p}_{\psi_f}} H_d + \hat{D}_{33}\nabla_{\hat{p}_{\psi_c}} H_d \\ &+ \nabla_{\hat{\psi}_c} H - c_1 J_3 (\hat{\psi}_c - \hat{\psi}_c^*) - c_2 J_4 (l_p - l_p^*) \\ &- c_3 J_5 (\phi - \phi^*)]), \end{aligned}$$

where $\nabla_{\hat{v}_0} H$, $\nabla_{\hat{\psi}_f} H$ and $\nabla_{\hat{\psi}_c} H$ are given by:

$$\begin{bmatrix} \nabla_{\hat{v}_0} H \\ \nabla_{\hat{\psi}_f} H \\ \nabla_{\hat{\psi}_c} H \end{bmatrix} = \begin{bmatrix} \hat{K}_{11} & \hat{K}_{12} & \hat{K}_{13} \\ \hat{K}_{12} & \hat{K}_{22} & \hat{K}_{23} \\ \hat{K}_{13} & \hat{K}_{12} & \hat{K}_{33} \end{bmatrix} \begin{bmatrix} \hat{v}_0 \\ \hat{\psi}_f \\ \hat{\psi}_c \end{bmatrix} + \begin{bmatrix} 0 \\ 0 \\ \nabla_{\hat{\psi}_c} H_f \end{bmatrix} + \begin{bmatrix} 0 \\ 0 \\ \nabla_{\hat{\psi}_c} H_e \end{bmatrix}.$$

Based on (20), and assuming $\alpha_1 = \alpha_3 = I_\ell$, $\alpha_2 = \alpha_4 = 0$, and $r_{55} = c_5 I_\ell$ with $c_5 \in \mathbb{R}_+$, the control law is expressed as:

$$\begin{aligned} \beta(x) = (R_e^{-1}\gamma(\hat{\psi}_c))^\dagger [&L_{ind}^{-1}\phi + R_e^{-1}C^{-1}Q - \nabla_{\hat{p}_{\psi_c}} H_d \\ &- c_1(\hat{\psi}_c - \hat{\psi}_c^*) - c_5 c_4 (Q - Q^*)], \end{aligned} \tag{26}$$

where the design parameters include the constants c_1, c_4, c_5, and the equilibrium states $\hat{\psi}_c^*$ and Q^*. These equilibrium states are derived from Figures 5 and 6 to ensure the desired tip position h_{tip} is achieved, while the constants c_1, c_4 and c_5 are selected to meet desired performance specifications.

Discussion: Similar to its counterpart designed for the low-scale model in (Cisneros et al., 2024), the control law in (26) shares several characteristics. Notably, $\beta(x)$ retains a structure and dimensionality equivalent to that derived for the low-scale model, demonstrating that expanding the state space in the large-scale model does not add complexity to the control law when equivalent closed-loop structures and energies are imposed. However, some limitations are also shared. As in the low-scale setting, the parameter r_{33} (along with r_{11} and r_{22} in the large-scale setting) cannot be directly assigned. These parameters are determined by the imposed closed-loop structure and desired energy function. Consequently, verifying whether the closed-loop system is asymptotically stable at the desired equilibrium x^* requires ensuring that $R_d(x) \geq 0$, which is a non-trivial task. Nevertheless, the degrees of freedom associated with r_{12}, r_{13} and r_{23} can be exploited to fulfill this condition. Moreover, an alternative approach to address these challenges in stability analysis is to consider different configurations of the matrices J_d and R_d, as well as a different energy function H_d with minimum at x^*. These choices would naturally result in different control laws $\beta(x)$. This flexibility offers promising opportunities for refining control design and enhancing performance, which will be explored in future work.

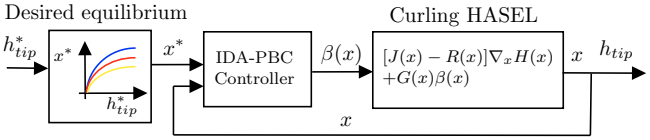

Fig. 7. Closed-loop scheme with the controller $u = \beta(x)$.

4. NUMERICAL SIMULATIONS

In this section, the proposed controller (26) is implemented in simulations following the scheme shown in Figure 7. The physical parameters of the large-scale curling HASEL actuator model are listed in Table 1. For further details on the experimental identification of these parameters and the discretization process, please refer to (Ponce et al., 2024).

Considering as set points the desired tip positions, from Figures 5 and 6 we obtain the controllers's parameters $\hat{\psi}_c^*$ and Q^*, respectively. The other design parameters are

Symbol	Value	Units	Definition
L_p	0.015	m	Length of top film
L_v	0.01	m	Length of bottom film
L_e	0.01	m	Length of electrodes
X_h	0.002	m	Chamber high
ϵ_r	2.2	F/m	Relative permittivity
ϵ_0	8.854×10^{-12}	F/m	Vacuum permittivity
w	0.075	m	Actuator width
h_f	18×10^{-6}	m	Film thickness
R_i	10	Ω	Resistance
r_i	20	Ω	Resistance
L_i	140	F	Inductance
K_l^i	300	N/m	Stiffness
K_f^i	3	Nm/rad	Stiffness
α	30.1256	-	Gain parameter
β	2.343	-	Gain parameter
η	diag(0.1, 0.28, ... 0.46, 0.64, 0.82, 1)	-	Correction factors
h	0.2×10^{-3}	m	Beam's height
L	0.12	m	Beam's length
A	1.5×10^{-5}	m^2	Cross-section area
I	5×10^{-14}	m^4	Cross-section inertia
ρ	2000	kg/m^3	Density
E	2.6583×10^7	Pa	Young's modulus
a_M	5×10^{-6}	-	Damping coefficient
a_K	2.338×10^{-2}	-	Damping coefficient

Table 1. Physical parameters of the large-scale model.

chosen as: $c_1 = 3$ [Nm/rad], $c_4 = 1 \times 10^{10}$ [1/C], and $c_5 = 0.1$ [1/Ω]. Figure 8 shows the results of the tip position in closed-loop, along with the magnitude of the control input.

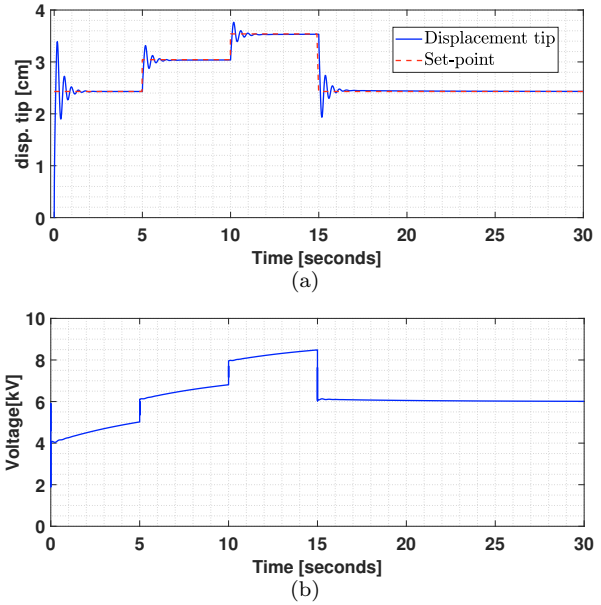

Fig. 8. (8a) Controlled tip position. (8b) Input signal.

Figure 8a shows that the actuator swiftly and accurately tracks the set-point reference position using the proposed controller, effectively compensating for the drift effect. Similarly, Figure 8b shows that, as expected, the controlled voltage remains within the acceptable range of 0 [kV] to 10 [kV], adhering to the actuator's physical constraints, despite the overshoot observed in the closed-loop response. Observe also in Figure 8b that, after the reference change at Time = 15 [seconds], the control input decreases slightly, yet no drift effect is observed in Figure 8a. This behavior is explained by a phenomenon known as re-actuation (Rumley et al., 2022). When the reference decreases, the inductor in the model begins to discharge, effectively acting as an internal source that contributes to mitigating the drift effect.

5. CONCLUSIONS

The IDA-PBC controller presented in (Cisneros et al., 2024) is extended to a large-scale model of a Curling HASEL actuator. The actuator tip successfully reaches the desired position, and the drift effect is effectively mitigated. As in the low-scale setting, the controller's dimension primarily depends on the number of HASEL pouches connected to the beam. Thus, if the number of chambers does not increase, the controller dimension remains unchanged.

As future work, the integration of multiple HASEL actuators into flexible structures to achieve complex deformation patterns will be explored, particularly in the context of distributed actuation for shape control. In addition, the work will focus on analyzing the stability of the controller and investigating alternative asymptotically stabilizing strategies for simultaneous position and force control, with particular attention to mitigating drift effects. The performance of the resulting closed-loop systems will be validated through experiments, for which appropriate state observers must be designed.

REFERENCES

Cisneros, N., Wu, Y., Rabenorosoa, K., and Le Gorrec, Y. (2024). Port-Hamiltonian modeling and control of a curling HASEL actuator. *IFAC-PapersOnLine*, 58(6), 143–148.

Duindam, V., Macchelli, A., Stramigioli, S., and Bruyninckx, H. (2009). *Modeling and control of complex physical systems: the port-Hamiltonian approach*. Springer Science & Business Media.

Hess, I. and Musgrave, P. (2024). A continuum soft robotic trout with embedded HASEL actuators: design, fabrication, and swimming kinematics. *Smart Materials and Structures*, 33(10), 105043.

Kazemipour, A., Hinchet, R., and Katzschmann, R.K. (2024). Stretchable electrohydraulic artificial muscle for full motion ranges in musculoskeletal antagonistic joints. *arXiv preprint arXiv:2409.11017*.

Kellaris, N., Gopaluni Venkata, V., Smith, G.M., Mitchell, S.K., and Keplinger, C. (2018). Peano-HASEL actuators: Muscle-mimetic, electrohydraulic transducers that linearly contract on activation. *Science Robotics*, 3(14).

Kellaris, N., Rothemund, P., Zeng, Y., Mitchell, S.K., Smith, G.M., Jayaram, K., and Keplinger, C. (2021). Spider-inspired electrohydraulic actuators for fast, soft-actuated joints. *Advanced Science*, 8(14), 2100916.

Ortega, R., van der Schaft, A., Maschke, B., and Escobar, G. (2002). Interconnection and damping assignment passivity-based control of port-controlled Hamiltonian systems. *Automatica*, 38(4), 585–596.

Ponce, C., Cisneros, N., Wu, Y., Rabenorosoa, K., Le Gorrec, Y., and Ramirez, H. (2024). Port-Hamiltonian modeling of large-scale curling HASEL actuators. *IFAC-PapersOnLine*, 58(21), 238–243.

Prodromakis, T. and Papavassiliou, C. (2009). Engineering the Maxwell-Wagner polarization effect. *Applied Surface Science*, 255(15), 6989–6994.

Rothemund, P., Kellaris, N., Mitchell, S.K., Acome, E., and Keplinger, C. (2021). HASEL artificial muscles for a new generation of lifelike robots—recent progress and future opportunities. *Advanced Materials*, 33(19), 2003375.

Rumley, E., Rothemund, P., Zhang, S., Kellaris, N., and Keplinger, C. (2022). Characterization of charge retention effects in HASEL actuators. In *Electroactive Polymer Actuators and Devices (EAPAD) XXIV*, PC120420B. SPIE.

Sanchez-Tamayo, N., Yoder, Z., Rothemund, P., Ballardini, G., Keplinger, C., and Kuchenbecker, K.J. (2024). Cutaneous electrohydraulic (CUTE) wearable devices for pleasant broad-bandwidth haptic cues. *Advanced Science*, 2402461.

Sîrbu, I.D., Preninger, D., Danninger, D., Penkner, L., Schwödiauer, R., Moretti, G., Arnold, N., Fontana, M., and Kaltenbrunner, M. (2023). Electrostatic actuators with constant force at low power loss using matched dielectrics. *Nature Electronics*, 6(11), 888–899.

Tripathi, A.S., Jiao, C., Hubracht, A.L.P., Paschew, G., Marschner, U., Henke, E.F.M., Maas, J., and Richter, A. (2024). Miniaturization of HASEL actuators for next-generation applications. In *ACTUATOR 2024*, 237–240.

Volchko, A., Mitchell, S.K., Scripps, T.G., Turin, Z., and Humbert, J.S. (2024). Robust control of electrohydraulic soft robots. *Frontiers in Robotics and AI*, 11, 1333837.

Xiong, Q., Zhou, X., Li, D., and Yeow, R.C.H. (2024). AC-driven series elastic electrohydraulic actuator for stable and smooth displacement output. *arXiv preprint arXiv:2401.13941*.